



# Performance of miniaturized atomic clocks in static laboratory and dynamic flight environments

Ankit Jain<sup>1</sup> · Thomas Krawinkel<sup>1</sup> · Steffen Schön<sup>1</sup> · Andreas Bauch<sup>2</sup>

Received: 25 May 2020 / Accepted: 18 September 2020 / Published online: 13 October 2020  
© The Author(s) 2020

## Abstract

Miniaturized atomic clocks with high frequency stability as local oscillators in global navigation satellite system (GNSS) receivers promise to improve real-time kinematic applications. For a number of years, such oscillators are being investigated regarding their overall technical applicability, i.e., transportability, and performance in dynamic environments. The short-term frequency stability of these clocks is usually specified by the manufacturer, being valid for stationary applications. Since the performance of most oscillators is likely degraded in dynamic conditions, various oscillators are tested to find the limits of receiver clock modeling in dynamic cases and consequently derive adequate stochastic models to be used in navigation. We present the performance of three different oscillators (Microsemi MAC SA.35m, Spectratime LCR-900 and Stanford Research Systems SC10) for static and dynamic applications. For the static case, all three oscillators are characterized in terms of their frequency stability at Physikalisch-Technische Bundesanstalt, Germany's national metrology institute. The resulting Allan deviations agree well with the manufacturer's data. Furthermore, a flight experiment was conducted in order to evaluate the performance of the oscillators under dynamic conditions. Here, each oscillator is replacing the internal oscillator of a geodetic-grade GNSS receiver and the stability of the receiver clock biases is determined. The time and frequency offsets of the oscillators are characterized with regard to the flight dynamics recorded by a navigation-grade inertial measurement unit. The results of the experiment show that the frequency stability of each oscillator is degraded by about at least one order of magnitude compared to the static case. Also, the two quartz oscillators show a significant g-sensitivity resulting in frequency shifts of  $-1.2 \times 10^{-9}$  and  $+1.5 \times 10^{-9}$ , respectively, while the rubidium clocks are less sensitive, thus enabling receiver clock modeling and strengthening of the navigation performance even in high dynamics.

**Keywords** Allan variance · Miniaturized atomic clocks · Frequency stability · Flight navigation · GNSS

## Introduction

Positioning, navigation and timing (PNT) applications using global navigation satellite system (GNSS) measurements require at least four satellites in view to solve for three-dimensional coordinates and a *receiver clock bias*. This bias must be estimated to synchronize the receiver's timescale with the GNSS timescale. The same applies to the satellite timescales to which the GNSS measurements refer. Corrections for the corresponding *satellite clock biases* can be extracted from either the navigation message transmitted by the satellites or clock products provided by the International GNSS Service (IGS, Johnston et al. 2017). Furthermore, the receiver clock bias has to be estimated at every measurement epoch because of the poor accuracy and limited long-term stability of the receiver's internal quartz oscillator. Replacing the latter by a more stable external one, such as

---

The authors do not attempt to recommend any of the instruments under test. It is noted that the performance of the equipment presented in this paper depends on the particular environment and the individual instruments in use. Other instruments of the same type or the same manufacturer may show a different behavior. The reader is, however, encouraged to test his own equipment to identify the system performance with respect to a particular application.

---

✉ Ankit Jain  
jain@ife.uni-hannover.de

<sup>1</sup> Institut für Erdmessung, Leibniz Universität Hannover, Hannover, Germany

<sup>2</sup> Physikalisch-Technische Bundesanstalt, Braunschweig, Germany

an atomic clock, enables a technique called receiver clock modeling (RCM) as proposed by Misra et al. (1995). Here, instead of being estimated on an epoch-by-epoch basis, the receiver clock bias is modeled over time intervals during which the clock noise is smaller than the noise of the GNSS observable in use.

This approach is especially beneficial in kinematic single-point positioning when using pseudorange observations and a miniaturized atomic clock (MAC), like a chip-scale atomic clock (CSAC), as shown by Weinbach and Schön (2011) and Krawinkel (2018). It also enables the estimation of the user position with only three satellites in view by using the concept of clock coasting, as shown by Sturza (1983), Knable and Kalafus (1984) and Krawinkel and Schön (2016).

With the advancements in miniaturization, several cost-effective and compact atomic clocks were developed and are now available in the market. Moreover, the frequency stability of such an atomic clock is better than that of a typical temperature-compensated crystal oscillator (TCXO), which are typically used in geodetic-grade GNSS receivers. The low cost, small form factor and high frequency stability of such atomic clocks make them usable in kinematic GNSS applications. Results by Krawinkel and Schön (2016) from a test drive experiment with several MACs showed that the precision of the vertical coordinate and velocity estimates could be improved by about 50–70% when RCM is applied. The single-point positioning solution also becomes more reliable and robust against outliers thanks to smaller minimal detectable biases (Teunissen 1997). Similarly, an improvement in the precision of the up-coordinates of about 75% is reported in two different flight trajectory simulation studies carried out by Krawinkel and Schön (2018) and Jain and Schön (2019), respectively. In both cases, the receiver clock biases are modeled in a physically meaningful way according to Kasdin (1995); however, the impact of external influences like vibrations and vehicle dynamics is not considered.

In general, oscillators are sensitive to accelerations such as vibrations, mechanical shock or even steady acceleration. Due to these external influences, there is a shift in the nominal frequency of the oscillator or an increased phase noise. As explained by Filler (1988) and Vig et al. (1992), the frequency shift depends upon the acceleration sensitivity of the oscillator. Assuming the sensitivity of a 10 MHz oscillator is  $1 \times 10^{-9}$  per one gravitational acceleration unit  $g$  amounting to approximately  $9.8 \text{ m/s}^2$ , and with typical root-mean-square accelerations of different aircrafts being in the range of 0.02–5  $g$ , the frequency shift would be about 0.2–50 mHz, respectively. Hence, in applications which mainly rely on the low phase noise of the oscillator, the performance of the overall system is degraded.

The performance of three different rubidium oscillators in varying gravity and magnetic field conditions in a laboratory setup and dynamic (flight test) case is explained in Van

Graas et al. (2013). Here, it is reported that the frequency offsets are degraded by an order of magnitude during the flight experiment compared to the laboratory setup. The specific names of the characterized oscillators are not mentioned in the article.

In different phases of a flight, the dynamics vary and they are particularly large during takeoff, turning and landing phases. Specifically, the response of the oscillator is noisier compared to the response in steady state. Hati et al. (2009) propose different techniques such as using low vibration-sensitive materials, vibration isolators with low frequency and active electronic vibration cancellation to suppress the phase noise generated by these dynamics. However, these measures increase the cost of the oscillator and make it larger in size. Hence, it is always beneficial to have prior knowledge about the oscillator's behavior in conditions in which it shall be applied so that the introduced errors can be modeled appropriately.

We present the performance analysis of two different miniaturized atomic clocks, namely a Microsemi MAC SA.35m and a Spectratime LCR-900, as well as a high-precision quartz oscillator, Stanford Research Systems (SRS) SC10. This is done both in a laboratory and in a dynamic environment, where the latter is being investigated by means of a flight experiment. At first, the frequency stability of the three oscillators in a laboratory environment is discussed. This also includes a subsection dedicated to temperature sensitivity for one of the oscillators. Then, the performance of the three oscillators is analyzed by means of a highly dynamic flight experiment. Also, the impact of different flight dynamics on the time and frequency offsets of the clocks is discussed. Finally, conclusions are drawn based on the clock performance in static and dynamic conditions.

## Clock characterizations

In this section, the individual frequency stability of two atomic clocks and one quartz oscillator is determined by comparing them to a frequency standard of significantly higher stability. Finally, spectral coefficients that can be used in a Kalman filter, for example, are derived thereof.

## Approach and measurement configuration

In order to correctly model the behavior of an oscillator, its spectral properties need to be determined first. One source of information is manufacturer's data. However, as shown by Krawinkel and Schön (2014), this information is often only given in relatively sparse temporal resolution and is also not necessarily representative of a particular oscillator. Another method to obtain the spectral characteristics is by comparing

it to an oscillator of at least one magnitude higher stability, for example an active hydrogen maser.

In this case study, such comparison measurements were carried out at the Physikalisch-Technische Bundesanstalt (PTB), Germany’s national metrology institute, at the end of October 2019. During this experiment, two rubidium clocks (Microsemi MAC SA.35m and Spectratime LCR-900), as well as an ovenized quartz oscillator (SRS SC10), were tested. The measurements were taken by means of different frequency counters (PikTime Systems T4100, SRS SR620, K + K KL-3400) using sampling intervals ranging from 0.1 to 100 s in order to cover different spectral bands of the oscillator output signals. Additionally, since quartz oscillators are well known to be sensitive to temperature changes, the SRS SC10 was also tested in that regard in a dedicated investigation. In all the cases, the reference signal for the comparison measurements was derived from either an ensemble solution of the cesium clocks at PTB or the official Coordinated Universal Time (UTC) signal, i.e. UTC(PTB) whose short-term frequency stability is that of an active hydrogen maser.

**Frequency stability**

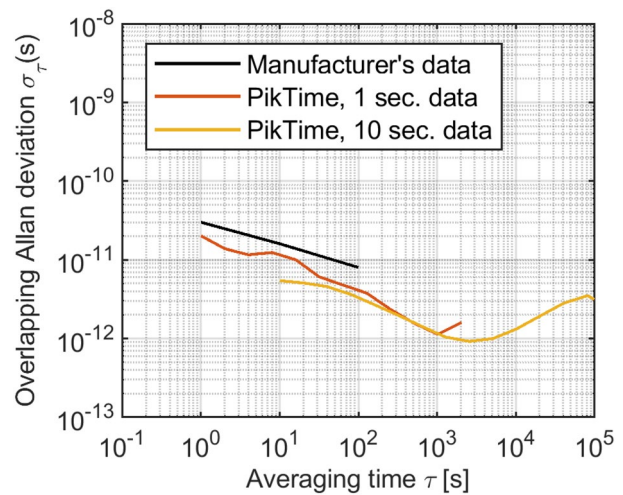
The common operand for analyzing the spectral characteristics of the three oscillators is the so-called fractional frequency deviations, as proposed by Riley (2008). These values are derived from different measurement parameters of the frequency counters, such as raw frequency measurements and phase residuals. Prior to computing the Allan deviation (ADEV, Allan 1987) of the measurements, the latter are converted to fractional frequency deviations if necessary and checked for outliers and data gaps. Furthermore, deterministic effects like frequency offset and drift are removed from the time series. Subsequently, the ADEV values are converted manually to the so-called  $h_\alpha$ -coefficients according to Barnes et al. (1971), which can be applied, for example, in a Kalman filter in order to model the spectral behavior of the investigated oscillators correctly (Krawinkel and Schön 2016). Each coefficient represents a distinct noise process so that their sum approximates the overall frequency stability of an oscillator and is given as follows:

$$S_y(f) = \sum_{\alpha=-2}^2 h_\alpha f^\alpha \tag{1}$$

where  $S_y(f)$  is the power spectral density of the fractional frequency deviations of the oscillator,  $f$  is the Fourier frequency and  $h_\alpha$  is the intensity coefficient of different noise processes denoted by power law exponent  $\alpha$ . The derived coefficients for three noise processes present in the investigated oscillators are listed in Table 1.

**Table 1** Spectral coefficients of investigated oscillators ( $h_0$ : white frequency noise,  $h_{-1}$ : flicker frequency noise,  $h_{-2}$ : random walk frequency noise)

Oscillator	$h_0$	$h_{-1}$	$h_{-2}$
Microsemi MAC	$0.8 \times 10^{-21}$	$7.2 \times 10^{-25}$	$3.0 \times 10^{-29}$
Spectratime LCR-900	$2.5 \times 10^{-21}$	$6.5 \times 10^{-26}$	$0.2 \times 10^{-29}$
SRS SC10	–	$1.8 \times 10^{-24}$	$7.6 \times 10^{-27}$



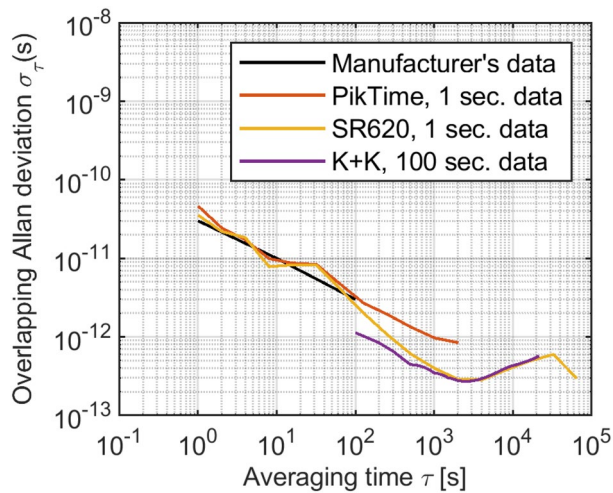
**Fig. 1** Frequency stability of the Microsemi MAC derived from different measurement time series. For more information about the different curves, we refer to Table 2

Figure 1 shows the frequency stability of our Microsemi MAC derived from two datasets with two different sampling intervals of one second and ten seconds, cf. Table 2. Obviously, both values at an averaging time  $\tau$  of ten seconds do not coincide, which can be attributed to some extent to the much higher sample size—and thus higher confidence level—of the ten-second measurements, especially at that particular averaging time ( $\tau = 10$  s). Furthermore, it is likely that the oscillator was not running as stably as it was during the ten-second measurements, which were taken a couple of hours after the one-second measurements without turning it off in between. From there, the two ADEV curves converge and are almost identical at  $\tau = 100$  s. Furthermore, the individually determined ADEV values suggest better frequency stability than specified by the manufacturer. The relatively unsettled behavior of the ten-second measurements leads to a slightly higher overall noise floor in terms of an ADEV of  $1 \times 10^{-12}$ .

The ADEV values of our Spectratime LCR-900 depicted in Fig. 2 display good agreement with manufacturer’s ADEV data, which are only given for short-term averaging times up to 100 s. In our case, the long-term stability of the oscillator varies between the corresponding datasets since slightly

**Table 2** Measurement configurations of oscillator comparisons (CCE: cesium clock ensemble)

Oscillator	Sampling interval (s)	Measurement duration (s)	Reference signal	Measurement device	Depiction, line color
Microsemi MAC	1	10,000	UTC(PTB)	PikTime Systems T4100	Fig. 1, red
Microsemi MAC	10	514,000	UTC(PTB)	PikTime Systems T4100	Fig. 1, yellow
Spectratime LCR-900	1	10,000	UTC(PTB)	PikTime Systems T4100	Fig. 2, red
Spectratime LCR-900	1	222,200	UTC(PTB)	SRS SR620	Fig. 2, yellow
Spectratime LCR-900	100	172,600	CCE	K+K KL-3400	Fig. 2, purple
SRS SC10	0.1	1,000	CCE	K+K KL-3400	Fig. 3, red
SRS SC10	1	86,400	CCE	K+K KL-3400	Fig. 3, yellow
SRS SC10	10	345,600	CCE	K+K KL-3400	Fig. 3, purple
SRS SC10	100	465,400	CCE	K+K KL-3400	Fig. 4, blue



**Fig. 2** Frequency stability of Spectratime LCR-900 derived from different measurement time series. For more information about the different curves, we refer to Table 2

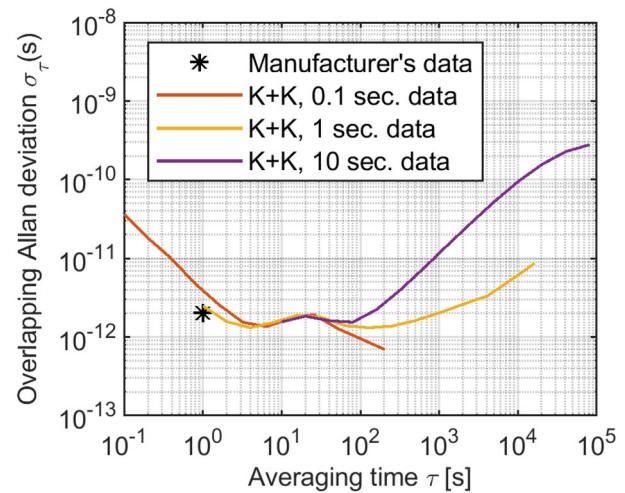


**Fig. 3** Frequency stability of SRS SC10 derived from different measurement time series. For more information about the different curves, we refer to Table 2

different ADEV values are determined for averaging times greater than 100 s. Because of its overall permanence, the one-second phase residual measurements depicted in yellow provide the best insight into the short-term as well as the long-term spectral characteristics of this oscillator.

The long-term frequency stability of the SRS SC10 differs from application to application as shown in Fig. 3, which is to be expected from a quartz oscillator. However, the estimated stability at one-second averaging time agrees very well with the manufacturer’s data. This should also make it applicable for GNSS receiver clock modeling for intervals up to 100 s, even when using carrier phase observations. On that note, for averaging times smaller than one second, the stability of this oscillator is degraded, which has to be considered in case 10 Hz GNSS measurements are being processed. However, from experience with the frequency counter K + K KL-3400 it is very likely that the ten-hertz measurements are dominated by the noise of

the counter itself, thus covering the behavior of the SC10 frequency signal. According to personal correspondence with the manufacturer of the counter, the noise amounts to ADEVs of  $3 \times 10^{-12}$  and  $1.5 \times 10^{-12}$  at averaging times of 1 s and 10 s, respectively.

**Temperature sensitivity**

In general, frequency stability is degraded when an oscillator is exposed to significant temperature changes, although differences can be observed depending on the type of oscillator (Microsemi 2018). This is especially true for crystal oscillators like, in the case at hand, the SRS SC10. In order to evaluate its temperature sensitivity, long-term comparison measurements were conducted within the scope of the laboratory experiment. Here, the temperature of the operating environment of the SC10 oscillator was also recorded. From both time series shown in Fig. 4, it can be seen that

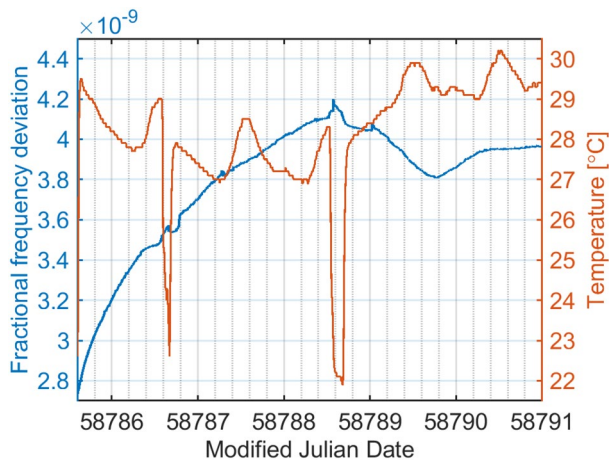


**Fig. 4** Fractional frequency deviations of the SRS SC10 and simultaneous room temperature readings. For more information about the fractional frequency deviation curve, we refer to Table 2

the oscillator frequency shifts whenever a (significant) temperature change occurs. This is very prominently visible around the times of Modified Julian Date (MJD) 58786.7 and 58788.7. Here, an increase in temperature leads to a decrease in frequency. These two pronounced events, i.e., drops in temperature, were caused by opening the windows of the laboratory for a couple of minutes. This means that also the humidity changed, but since that was not recorded, we cannot elaborate on it. Apart from that, the frequency deviations also vary independent of temperature changes, which can be seen from MJD 58789 to 58791.

## Flight experiment

In order to compute the frequency stability of the three oscillators in a highly dynamic environment and compare it with the static case, a flight experiment was conducted. The measurement setup, details of the flight experiment, analysis strategy and the corresponding results are described in this section.

### Measurement setup

The measurement configuration of the flight experiment is shown in Fig. 5. It consisted of four geodetic-grade JAVAD GNSS receivers of type Delta TRE-G3T(H), which were all running the same firmware version. In addition to the four receivers, there were three external atomic clocks, IGI's AEROcontrol unit (IGI 2020) and an active GNSS splitter, which was connected to the Antcom G5 antenna placed at the top of the aircraft fuselage. The internal circuitry of three receivers was each driven by one of the same three external oscillators presented in Sect. 2. Contrary to this, the fourth

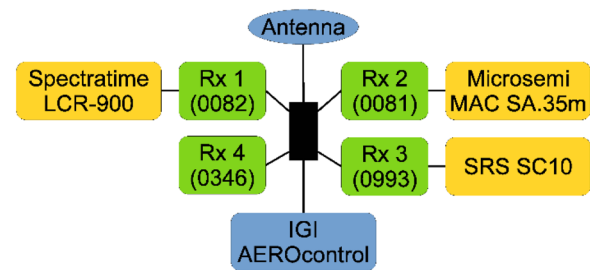


**Fig. 5** Flight experiment measurement configuration consisting of an active signal splitter (black), four JAVAD receivers (green), three external oscillators (yellow) as well as an Antcom G5 antenna and a GNSS/IMU unit (blue)

receiver was driven by its internal TCXO. The IGI AEROcontrol unit consists of a navigation-grade inertial measurement unit (IMU) combined with a high-precision Septentrio GNSS receiver. From the data captured with this instrument, a precise kinematic reference trajectory was computed for the complete duration of the flight experiment. Except for the GNSS antenna, all of the measurement equipment was fixed within a camera sensor pod.

Inside the aircraft, this sensor pod was placed on a passively dampened aerial photogrammetry mount as shown in Fig. 6. The passive dampening on the mount reduces the impact of sudden jerks, mechanical shocks and vibrations on the external oscillators and prevents them from potentially permanent damage.

### Flight maneuver details

The flight experiment was conducted on October 7, 2019, for about three hours in the vicinity of Dortmund airport in Germany using a modified twin-engine Cessna 404 TITAN aircraft. All receivers recorded GNSS pseudorange, carrier phase and Doppler measurements with a sampling rate of 10 Hz. During the experiment, two very similar sets of flight maneuvers were performed at two different (ellipsoidal) height levels of about 650 m and 2800 m, respectively. One set of these maneuvers consists of a straight-and-level flight followed by flight turns with varying roll angles. The first straight-and-level flight starts moving from east to west and then back to east, continued by a straight-and-level flight line again from south to north and then back to south. After these flight paths, the flight turns with high dynamics were conducted. At first, two flight turns with maximum roll angles of  $+25^\circ$  and  $-25^\circ$  followed by two flight turns with roll angles of up to  $+58^\circ$  and  $-58^\circ$  were performed. All flight maneuvers conducted at a lower altitude ( $\sim 650$  m) are referred to as *phase 1*, whereas similar maneuvers carried out at an upper altitude ( $\sim 2800$  m) are labeled as *phase 2* of the flight experiment. The corresponding flight trajectory paths of both

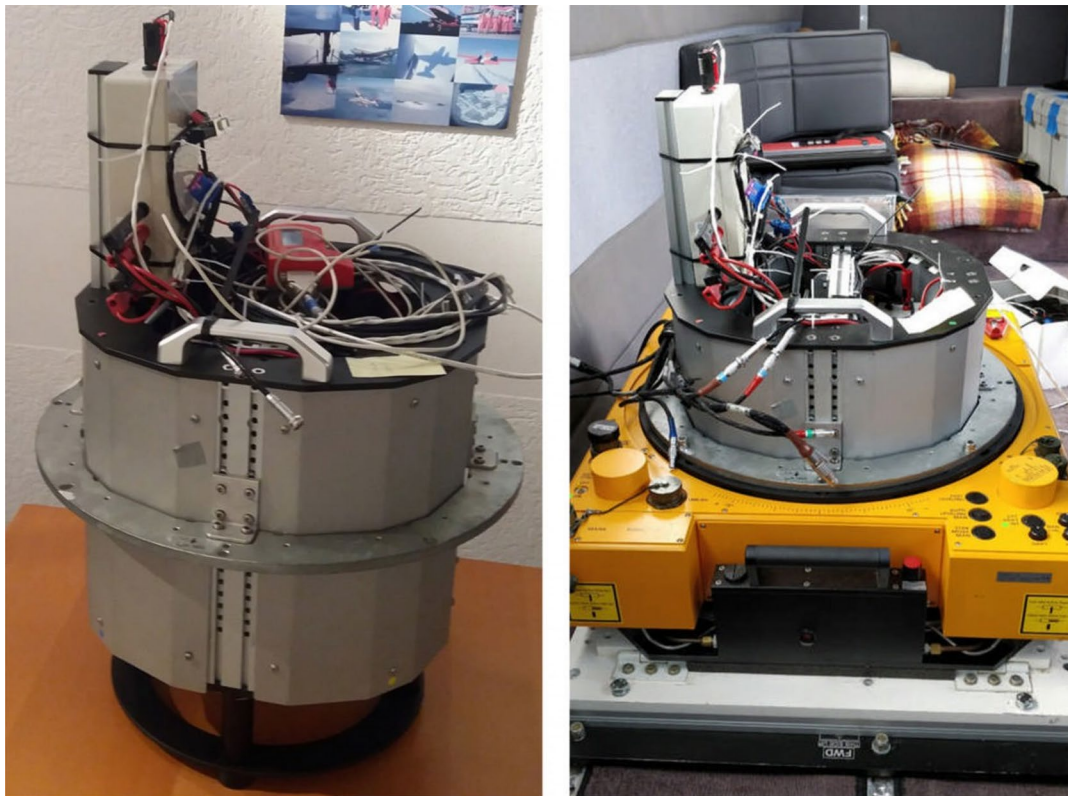


**Fig. 6** Camera sensor pod with different measurement devices fixed inside (left) and mounted inside the aircraft (right)

phases are shown in Fig. 7. There are four distinct points marked with different labels on each flight path in phase 1 and phase 2. The information about all the labeled points on both trajectories is summarized in Table 3 along with corresponding approximate GPS time stamps. In addition, the flight turns which involved high dynamics in phase 1 and phase 2 are depicted on the right-hand side of Fig. 7.

The flight dynamics (roll, pitch, yaw angles and total acceleration) measured by the AEROcontrol unit are shown in Fig. 8, where the black dashed lines correspond to the different marked points in the flight trajectory plots depicted in Fig. 7. The flight dynamics include roll angles up to  $\pm 59^\circ$  and pitch angles in the range of about  $-10^\circ$  to  $+10^\circ$ . The dynamics are the highest toward the end of both dynamic maneuvers where the aircraft is accelerating at magnitudes greater than  $2g$  and turning with the highest roll angles. The segments where the pitch angles are steadily increasing are part of the takeoff phase and the flight ascent phase to higher altitude. On the contrary, the phases where pitch angles are steadily decreasing refer to the flight descent phase to lower altitude and the landing phase. The phases wherein the yaw angles are constant belong to straight-and-level flight phases where the dynamics are not very high.

## Data processing

The basis of the following analysis is a reference trajectory computed by our contractor IGI in a relative positioning approach using GPS phase observations and measurements of an IMU combined in their AEROcontrol unit as well as GPS phase observations from a permanent reference station of the satellite positioning service of the German land survey (SAPOS).

Subsequently, estimation of the receiver clock time and frequency offsets uses a weighted least-squares approach implemented in our in-house MATLAB GNSS software. By using coordinates and velocities from the very precise reference trajectory and accurately modeling the remaining GNSS error sources such as satellite clock biases, tropospheric delay and relativistic effects, only the receiver clock time and frequency offsets are estimated epoch-wise using the ionospheric-free linear combination of GPS L1 and L2 P-code observations and GPS L1 Doppler observations, respectively. An elevation-dependent ( $\cos^2 E$ ) weighting matrix is used to account for the stochastic behavior of the observations. Data outliers are detected and rejected based on a simple threshold method. The satellite orbits and clock biases are computed using the precise orbit and

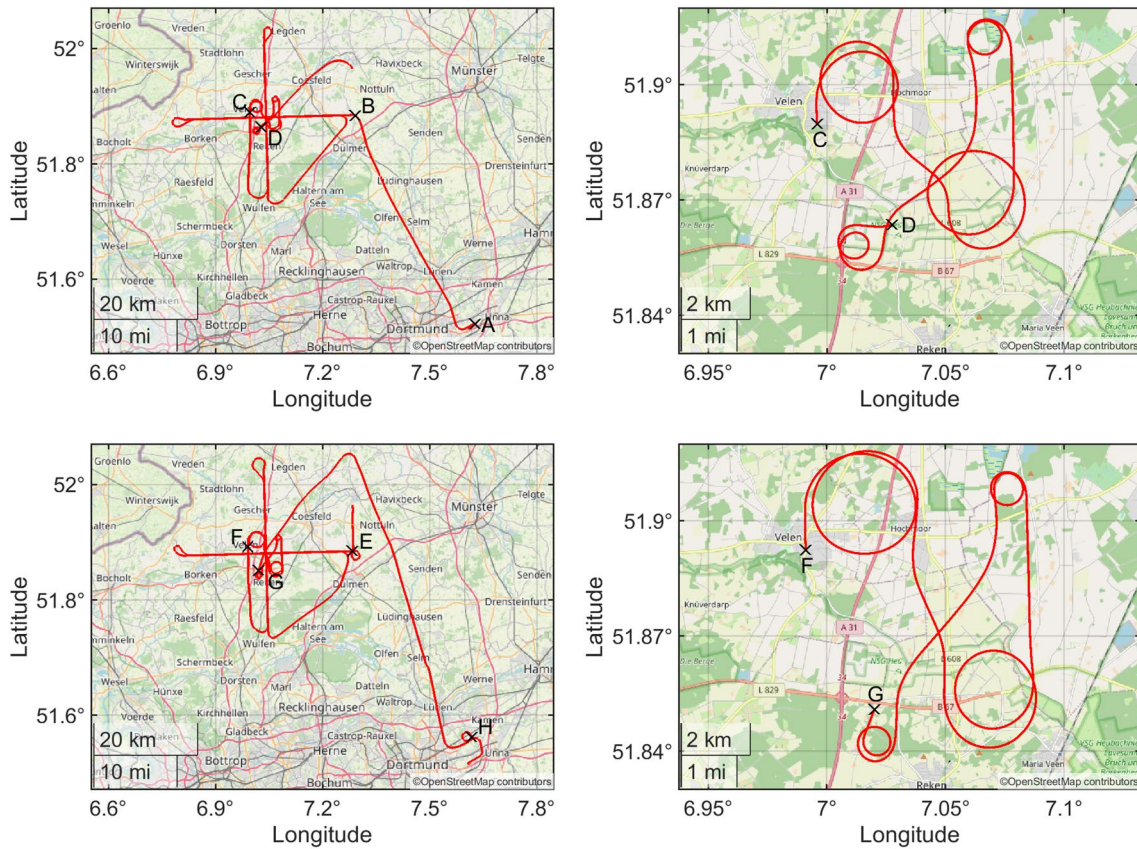


**Fig. 7** Flight trajectory ground tracks at two different altitudes of about 650 m (top) and 2800 m (bottom). A complete overview is given on the left; segments with high-dynamic turn maneuvers are shown on the right. More details about the marked points are listed in Table 3

**Table 3** Description of various flight segments

Marker label	Flight experiment details	Approximate GPS time
A	Start of takeoff phase	10:25:00
B	Start of straight-and-level phase at lower altitude	10:36:40
C	Start of flight maneuvers at lower altitude (first two turns with roll angles up to $\pm 25^\circ$ , later two steep turns with roll angles up to $\pm 58^\circ$ )	11:20:00
D	End of steep turn phase at lower altitude, start of ascent to higher altitude	11:32:30
E	Start of straight-and-level phase at higher altitude	11:42:15
F	Start of flight maneuvers at higher altitude (first two turns with roll angles of up to $\pm 25^\circ$ , later again two steep turns with roll angles up to $\pm 59^\circ$ )	12:26:30
G	End of steep turn phase at higher altitude, start of descent	12:39:40
H	Start of landing phase	12:58:45

clock products of the Multi-GNSS experiment (MGEX) of the IGS (Montenbruck et al. 2017). The signal delays due to the troposphere are accounted for by using the Vienna Mapping function (VMF1, Böhm et al. 2006). An elevation cutoff angle of five degrees is applied. As all the error sources except the receiver clock biases are removed from the pseudorange and Doppler observations, the estimates of clock time and frequency offsets are used to assess the

behavior of the oscillators. This approach is performed with an observation sampling rate of 10 Hz for each receiver.

**Quality of GNSS observations**

Figure 9 depicts the respective noise of GPS L1 Doppler observations recorded by the receiver connected to the Spectratime LCR-900 and the receiver driven by its internal

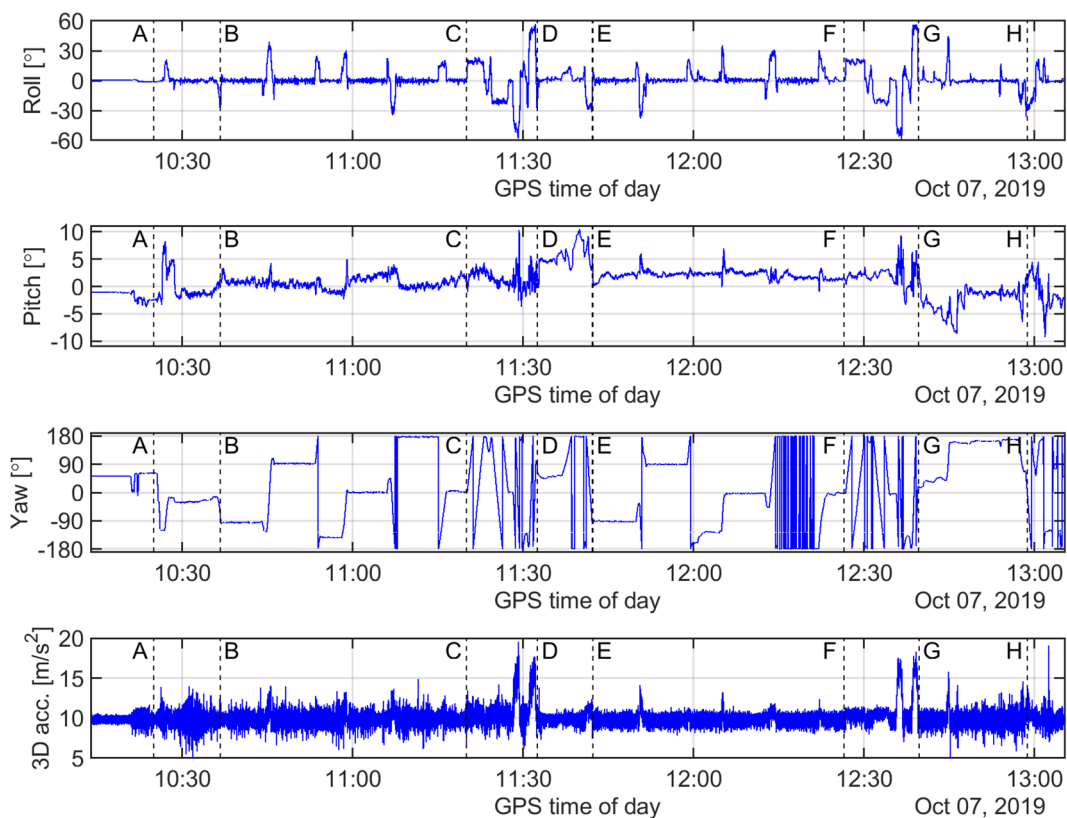


**Fig. 8** Flight dynamics as recorded by the IMU during the whole flight: Black dashed lines indicate different marked points, which are explained in Table 3. The marked point labels inserted in the last row apply to all time series

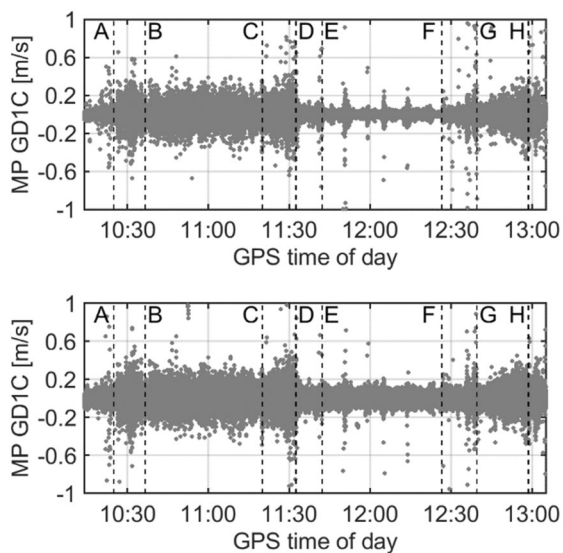


**Fig. 9** Remaining noise of GPS L1 Doppler (GD1C) observations computed by means of the so-called multipath linear combination, superimposed for a total of 13 satellites each as recorded by the receiver connected to Spectratime LCR-900 (top) and receiver driven by its internal oscillator (bottom)

TCXO (cf. Fig. 5). These noise levels are computed based on the so-called multipath linear combination wherein the L1 Doppler and time-differentiated carrier phase observations on L1 and L2 are used. The results of the receivers connected to Microsemi MAC and SC10, respectively, are similar to the result of the receiver plugged to the Spectratime LCR-900 as shown in the top row of Fig. 9. The overall noise levels of the L1 Doppler observations from different GPS satellites are very similar. In addition, it is observed that noise levels vary significantly with respect to flight altitude, i.e., at lower altitude (segment A–D), the noise level is much higher compared to that at higher altitude (segment D–G). The sudden noisy spikes seen in between markers D and G correspond to different flight turns (i.e., higher roll angles). It is also seen that the noise of the GPS L1 Doppler observations recorded by the receiver driven by its internal TCXO is higher compared to the other receivers, which were connected to different external oscillators.

The tracking of Doppler observations is primarily carried out using phase-locked loops (PLLs) in JAVAD Delta receivers. In order to investigate the different noise levels with respect to varying altitude and oscillator configuration (external or internal), different error sources contributing to the PLL noise are analyzed. According to Ward et al. (2006),



the four major are thermal noise, vibration-induced phase noise, Allan deviation oscillator phase noise and dynamic stress. The PLL order for all receivers was set to three, which means that the receiver can account for jerk stress, i.e., accelerated accelerations, and the PLL bandwidth was set to 25 Hz. Hence, the impact of thermal noise could be assumed similar for all receivers involved. Moreover, the dynamic stress error on the PLL can be neglected as there were no jerks experienced during the flight experiment.

The  $g$ -sensitivity of the oscillator and the frequency of external vibrations primarily affect the vibration-induced phase noise in the PLLs. The spectrogram of the accelerations recorded by the IMU during the flight experiment is shown in Fig. 10. At lower altitude (segment A–D), vibrations with considerable power density are prominent in the frequency range from about 0 to 60 Hz, whereas at higher altitude (segment D–G), the highest power density is visible in the range of 30–200 Hz. The vibration-induced phase noise is significantly higher for low-frequency than for higher-frequency vibrations as shown by Irsigler and Eissfeller (2002). Also, the amount of thermal turbulence experienced by the aircraft at lower altitudes is stronger than at higher altitudes. During the time when the experiment was conducted, there were clouds just below the flight path on the lower altitude, which results in higher turbulence. For the flight path at a higher altitude, the clouds were further below the aircraft, which results in a smoother flight, i.e., less thermal turbulence. Owing to the large vibration-induced phase noise and higher turbulence at a lower altitude, the noise level of Doppler observations is much higher.

The frequency instabilities of the oscillators result in noise referred to as Allan deviation oscillator phase noise.

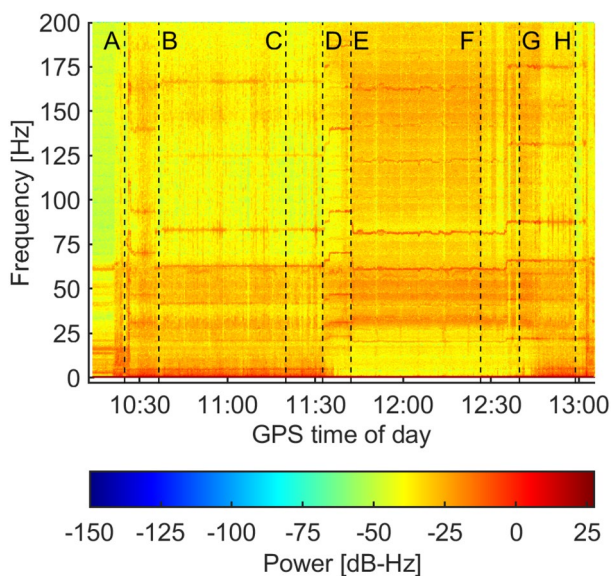


**Fig. 10** Spectrogram of acceleration recorded by the IMU

This type of phase noise is characterized as natural noise, and it is different from the vibration-induced phase noise. In the case of all three external oscillators used in the experiment, the frequency stability and  $g$ -sensitivity are much better compared to the internal TCXO within receiver no. 4 (Fig. 5). Hence, the noise levels of Doppler observations captured with this receiver are higher compared to the other three receivers.

The noise of all GPS L1 and L2 P-code observations recorded on all receivers is in the range of about  $\pm 1$  m (about 3.3 ns) along the complete flight trajectory. As the noise level is much higher for code observations, the effects of flight dynamics are not derivable from them. Moreover, the delay-locked loops (DLLs) of the receivers are aided through PLL, which removes all the dynamic stress errors as well.

### Clock performance

Figure 11 shows the ten-hertz clock time and frequency offsets of all four investigated oscillators. A linear trend is removed from all the time offset time series. In the case of the Microsemi MAC, higher-order effects still remain as the time series increases from about  $-170$  ns at the beginning of the flight to roughly  $95$  ns during the flight ascend phase to an upper altitude, before it gradually reduces to about  $-95$  ns toward the end of the flight experiment. Apart from a few noisy spikes during the roll maneuvers in phase 2 of the flight, the clock time offset apparently is not affected by these dynamics. The noise of the clock frequency offsets varies significantly with regard to the flight altitude. The noise level at the higher altitude (segment E–G) is about four times lower than that at lower altitude. This significant difference in the noise level corresponds to the behavior of Doppler observation noise. At lower altitudes, the clock frequency offsets do not exhibit substantial differences between straight-flight and turn maneuvers. However, at higher altitudes, the frequency offsets show some small spikes—compared to the overall noise level at that altitude (segment E–F)—that correspond to the flight turns with different roll angles. Among these spikes, the ones corresponding to roll angles of up to  $\pm 59^\circ$  in segment F–G are greater, thereby demonstrating the effects of high dynamics on the oscillator.

The estimated receiver clock frequency offsets are used to determine the frequency stability of a particular oscillator in a dynamic environment. The ADEV values are derived using the same method as during our laboratory investigations. Thus, Fig. 12 shows the frequency stability of all oscillators for five different flight segments. Also, white frequency noise is computed for the corresponding flight segments using the ADEVs at averaging time of 1 s. All these computed noise values are listed in Table 4. For the data captured from the start of the experiment until

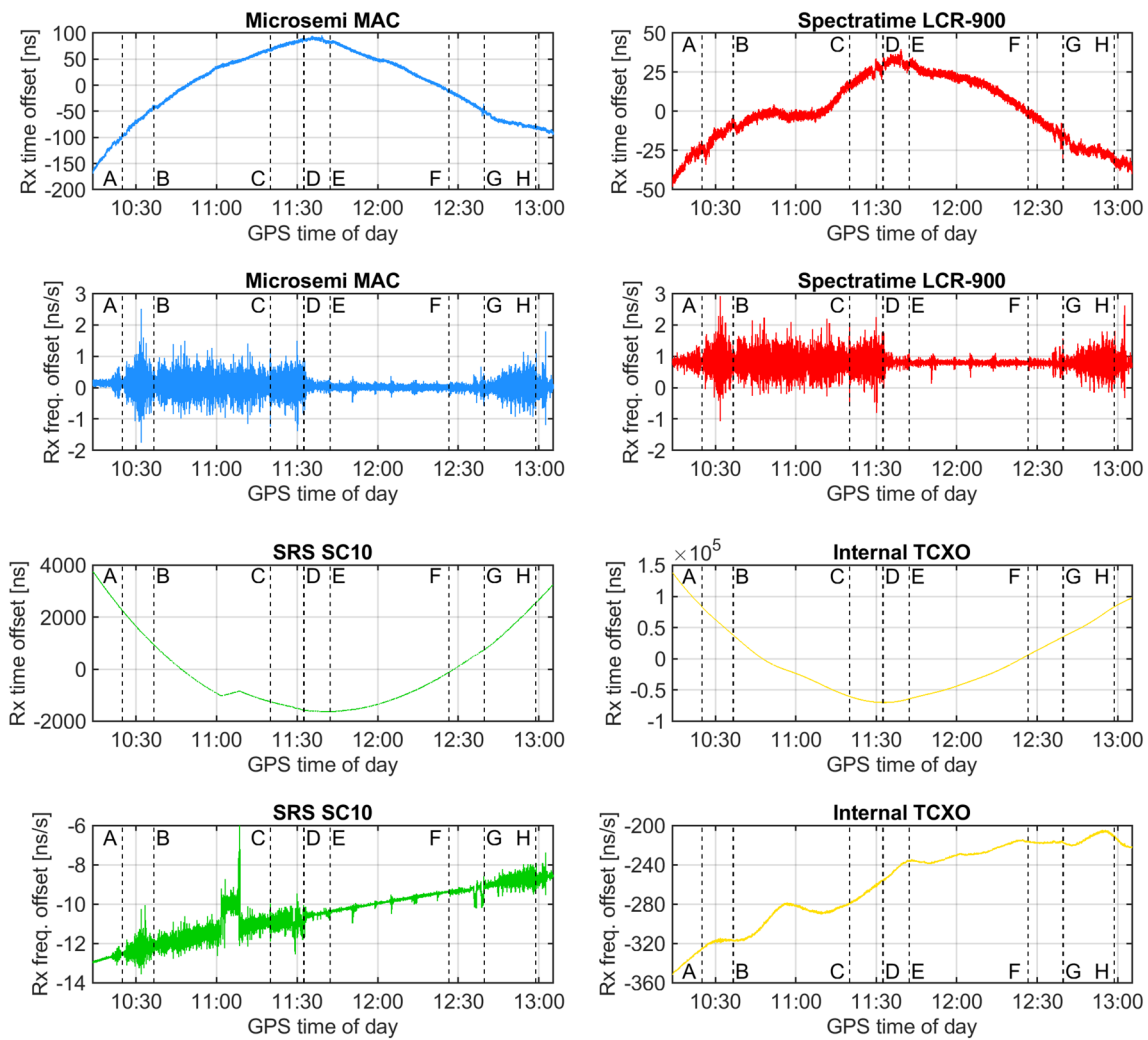


**Fig. 11** Receiver clock bias time series of time offset and frequency offset for all receivers. Offsets and drifts removed from time offset time series amount to: Microsemi MAC (235.509  $\mu$ s, 0.176  $\mu$ s/s),

Spectratime LCR-900 (421.563  $\mu$ s, 2.912  $\mu$ s/s), SRS SC10 (153.563  $\mu$ s, 37.596  $\mu$ s/s), internal TCXO (99.256  $\mu$ s, - 917.186  $\mu$ s/s)

point A (takeoff phase), the flight was static for about half of its total duration. Moreover, when the flight was in motion toward the runway, the velocity was almost constant. The Microsemi MAC ADEV values for the flight segment Start-A are better than the values specified by the manufacturer for averaging times up to 100 s. These values also agree well with the ADEV values computed for the static case, as shown in Fig. 1 for averaging time up to 10 s. At an averaging time of one second, the ADEV value for only segment E–F coincides with the manufacturer’s data. For averaging time greater than 10 s, the frequency stability is slightly better for straight-and-level flight segments B–C and E–F and worse for dynamic maneuver segments C–D and F–G, than the manufacturer’s data at both altitudes. Also, for flight segments B–C and C–D at a lower altitude, the frequency stability is worse compared

to stability at higher altitude in segments E–F and F–G at an averaging time of one second. Lastly, the ADEV values computed from the dynamic flight maneuvers in segments C–D and F–G are about one order of magnitude worse than the frequency stability computed in the static case, i.e., as shown in Fig. 1.

The clock time and frequency offsets of the receiver connected to the Spectratime LCR-900 show a smoother behavior compared to the Microsemi MAC, where the time offset ranges within about  $\pm 45$  ns. However, both time series are similar in a sense that they rise up until the same point—where the aircraft ascended to a higher altitude—and start decreasing from there. During the steep flight turns in both flight phases (cf. Table 3), the clock time offsets are seen oscillating sinusoidally, which can be associated with the high accelerations and roll angles on the LCR-900 oscillator.

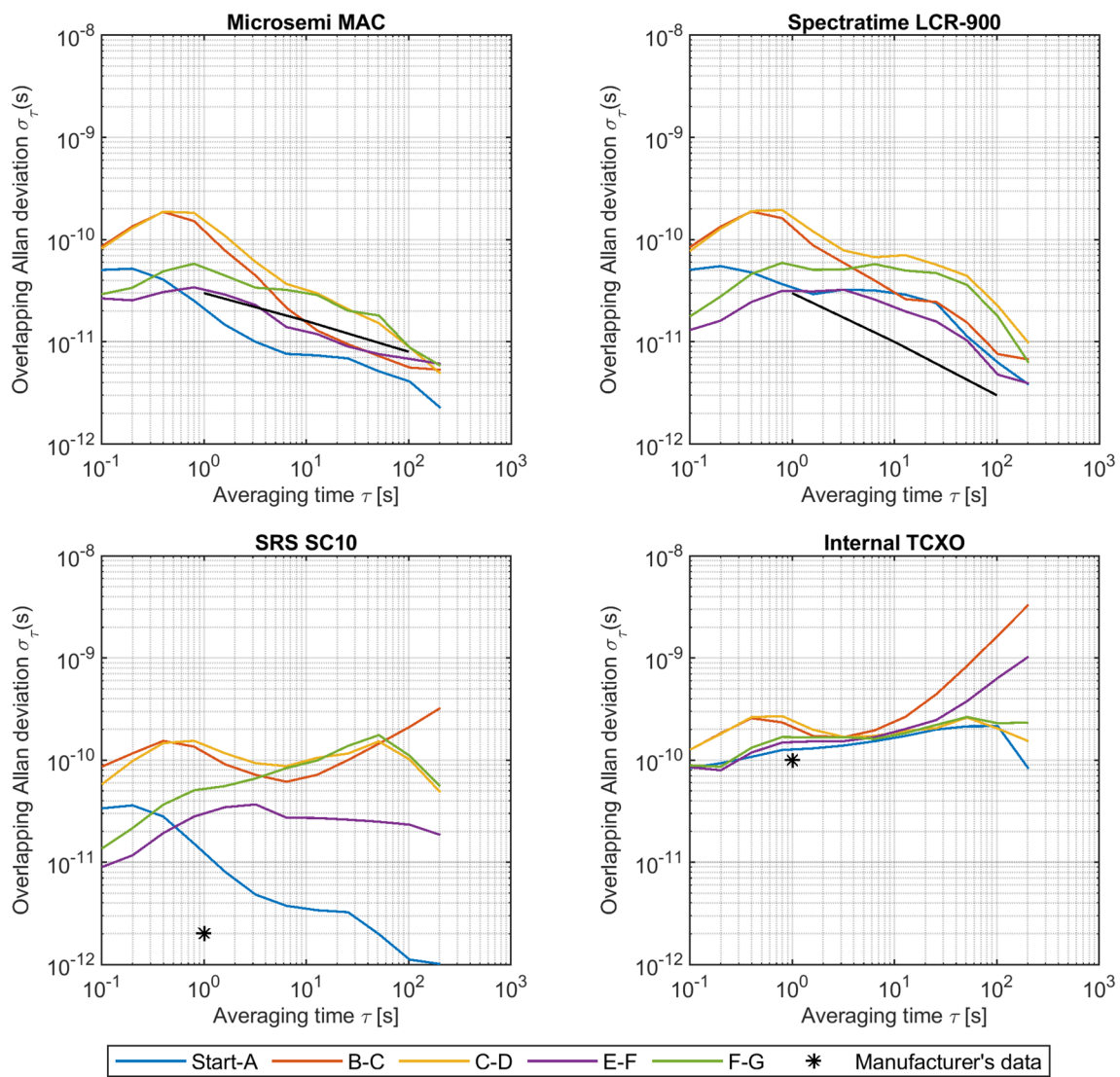


**Fig. 12** Frequency stability for all oscillators computed from receiver clock frequency offsets for different flight segments

**Table 4** White frequency noise for all the oscillators with regard to different flight segments and states derived from Allan deviations at an averaging time of one second as shown in Fig. 12

Flight segment	Microsemi MAC (ps)	Spectratime LCR-900 (ps)	SRS SC10 (ps)	Internal TCXO (ps)	Flight state
Start-A	21	34	12	127	Static followed by taxiing to runway
B–C	123	133	119	212	Mostly straight flight at lower altitude
C–D	155	167	141	244	High accelerations (steep turns) at lower altitude
E–F	32	31	30	150	Mostly straight at higher altitude
F–G	53	56	52	168	High accelerations (steep turns) at higher altitude

The frequency offsets show a behavior similar to the Microsemi MAC (cf. Fig. 11).

The ADEV value of our Spectratime LCR-900 at an averaging time of one second for flight segments Start-A and

E–F coincides with the values provided by the manufacturer. The computed frequency stability from the experiment data for dynamic maneuver flight segments C–D and F–G is about one magnitude worse compared to the manufacturer’s

data and compared to the results from the static case (cf. Fig. 2). At averaging time of one second, frequency stability behavior is similar to the MAC oscillator with regard to the different flight altitudes.

The ranges of the estimated clock time and frequency offsets of the receiver connected to the SRS SC10 are much higher compared to those of the two previously discussed rubidium clocks (cf. Fig. 11). The time series decreases from about + 3.7  $\mu\text{s}$  at the beginning of the flight experiment to about - 1.65  $\mu\text{s}$  prior to the beginning of straight-and-level flight in phase 2 after approximately 1.5 h. From there, the clock time offset increases to roughly 3.3  $\mu\text{s}$  until the end of the experiment. Also, two clock jumps are visible in both time series at around 10:58 and 11:05 GPS time of day. The effects induced by the flight dynamics are not visible in the clock time offsets due to the large range of the estimated clock time offsets. However, they can be seen in the frequency offsets. Here, also, the noise is higher when the flight is at lower altitudes and smaller at higher altitudes—similar to the behavior of the other two presented oscillators. The clock frequency offsets also show a significant linear drift of about + 1.6 ns per hour ( $\sim 0.4$  ps/s) throughout the whole experiment. Lastly, the impact of flight dynamics induced by steep turns in both flight phases is visible with sudden noisy spikes in segments C–D and F–G (cf. Table 3) in the clock frequency offsets.

The estimated frequency stability for the SC10 at one-second averaging time amounts to ca.  $1.24 \times 10^{-11}$  for the flight segment Start-A; it is the closest to static case estimated value (cf. Fig. 3) and manufacturer's data. The ADEV values for other flight segments at one second averaging time, particularly at the higher altitude (E–F and F–G), are about two orders of magnitude worse than the values provided by the manufacturer and the results obtained from the laboratory investigations. For averaging times greater than 1 s and less than 100 s, the frequency stability of segments B–C, C–D and F–G is about two orders of magnitude worse.

The clock time and frequency offset estimates of the receiver driven by its internal TCXO vary the most among all receivers. At the beginning of the flight, the value is about 138  $\mu\text{s}$  which gradually decreases to about - 70  $\mu\text{s}$ , somewhere during the flight ascend to the upper altitude (i.e., between D–E) phase. Further, the time offsets again gradually rise to about 100  $\mu\text{s}$  until the end of the experiment. The clock frequency offsets are also the highest among all the four receivers and show a significant drift, including both linear and quadratic terms. The effects of flight dynamics are not visible in the clock time and frequency offsets. The stability of the estimated frequency of the receiver offsets is shown in Fig. 12 for five different flight segments. At an averaging time of one second, the ADEV value for the takeoff phase (Start-A) agrees very well with the typical TCXO value. In addition, the ADEV values at one second

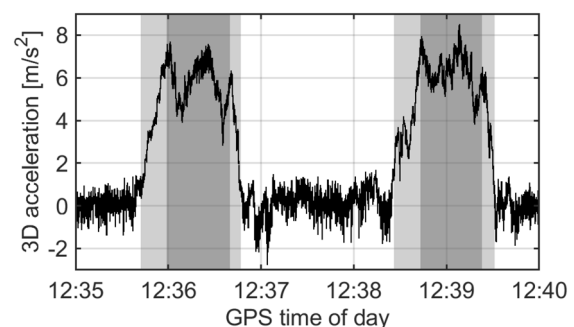
for segments E–F and F–G at higher altitudes are slightly better than the values at lower altitudes (B–C, C–D). This behavior corresponds to the noise level of Doppler observations shown in the bottom row of Fig. 9. For segments B–C and E–F that represent straight-and-level flights, the long-term frequency stability degrades for larger averaging times, which again is a drawback of a typical TCXO. The impact of dynamic maneuvers on the frequency stability of the oscillator is unnoticeable due to the high noise inside the frequency offsets.

### Impact of flight dynamics

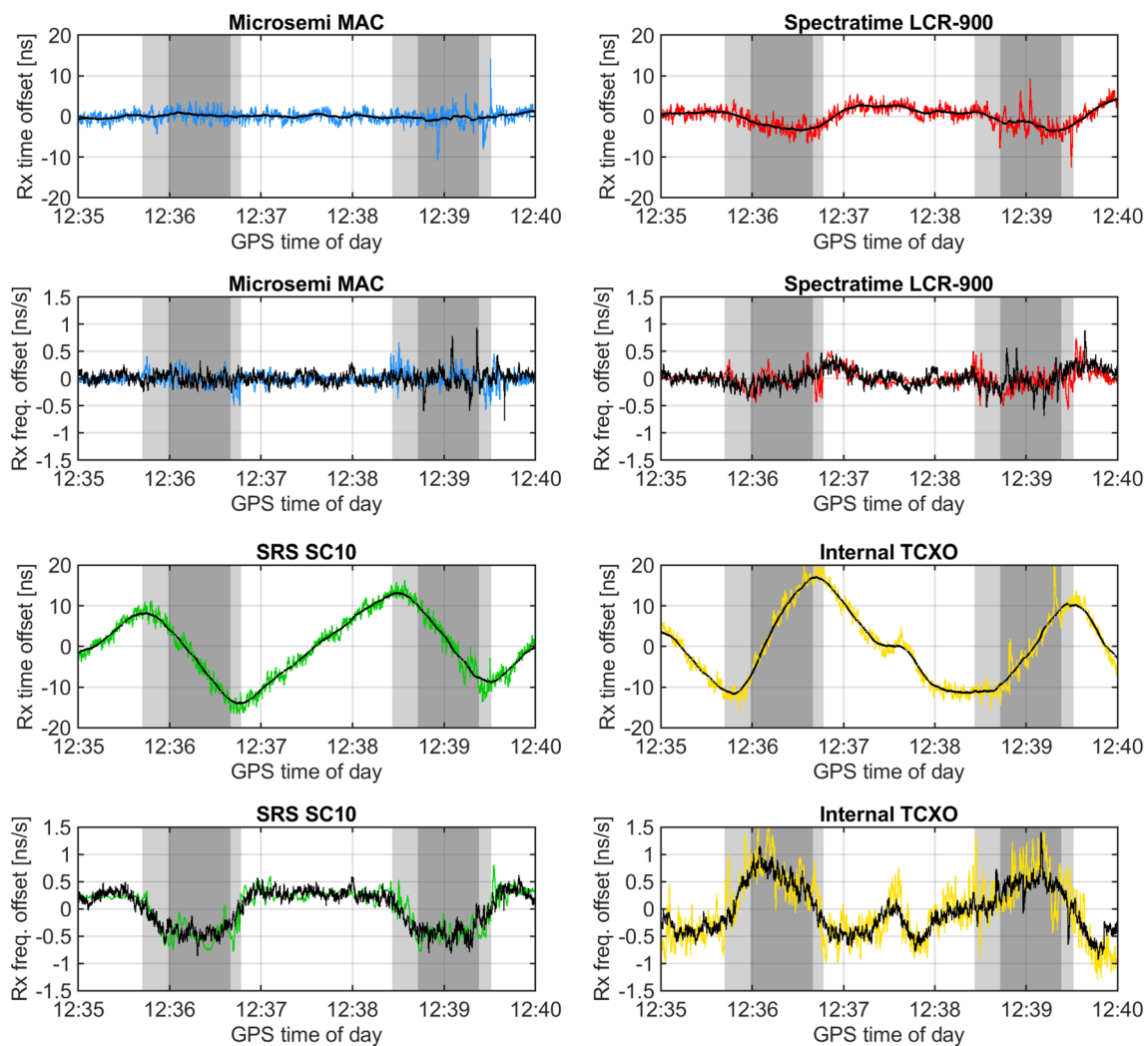
In order to analyze the influence of flight dynamics on the oscillators used in the experiment, the estimated receiver clock biases shown in Fig. 11 are investigated in relation to the aircraft accelerations recorded by the IMU. Two flight segments with very high accelerations stand out from Fig. 8, at the end of segments C–D and F–G, respectively. Therefore, we will have an in-depth look at segment F–G; nevertheless, the results derived from segment C–D are very similar.

Figure 13 shows the total acceleration of the aircraft during the two steep flight turns at the end of segment F–G (cf. Table 3). For this, the accelerations as recorded by the IMU are reduced by normal gravity acceleration according to the geodetic reference system 1980 (GRS80) model.

The receiver clock biases of segment F–G are depicted in Fig. 14. Here, quadratic and linear trends are removed from the time and frequency offsets, respectively. Furthermore, smoothed time offsets derived by means of a moving average filter—with a window length of 120 s—are also shown. Differentiating these smoothed time series with respect to the sampling rate of 10 Hz leads to additional frequency offsets. Black curves indicate both smoothed time offsets and frequency offsets derived from them. This approach reveals that the time offsets derived from pseudorange observations inherited the same effects as the frequency offsets derived



**Fig. 13** Total aircraft acceleration reduced by GRS80 normal gravity acceleration during two steep roll maneuvers in flight segment F–G. The gray-shaded areas indicate two acceleration phases



**Fig. 14** Receiver clock biases (time offset, frequency offset) of all receivers in flight segment F-G, where time offsets are quadratically detrended and frequency offsets are linearly detrended. Solid black lines in the time offset plots indicate smoothed moving average time

offsets, which differentiated in time result in the black frequency offsets. The gray-shaded areas correspond to the two acceleration phases as shown in Fig. 13

from Doppler observations. However, these effects are initially covered by the noise of the pseudorange observations and are also superimposed by severe drifts in case of the quartz oscillators.

When illustrating these clock biases as a function of aircraft acceleration, specific characteristic curves can be derived for each oscillator, as depicted in Fig. 15 by black lines. It can be seen that the clock biases of the Microsemi MAC show no dependency on the total acceleration, whereas the behavior of the other atomic clock, the Spectratime LCR-900, slightly does. This corresponds well with the  $g$ -sensitivity specified by the manufacturers as  $1.7 \times 10^{-10}$  (Microsemi MAC) and  $3.4 \times 10^{-10}$  (Spectratime LCR-900), respectively, according to personal communications and Spectratime (2014). The most pronounced

dependencies, however, are present inside the estimated clock biases of the two receivers, each connected to a quartz oscillator. In this case, an acceleration of  $+10 \text{ m/s}^2$  results in a frequency shift of  $-1.2 \text{ ns/s}$  (SRS SC10) and  $+1.5 \text{ ns/s}$  (internal TCXO), respectively. This also means that the user has to care that the oscillator is always operated within its specifications as stated by the manufacturer. The opposite positive and negative directions of sensitivity could be caused by different physical properties of the oscillators as well as their physical mounting inside the aircraft. Note that the characteristic curves computed for the time offsets of the quartz oscillators show no acceleration dependency since the input time series are superimposed by severe drifts (cf. third row of Fig. 14).

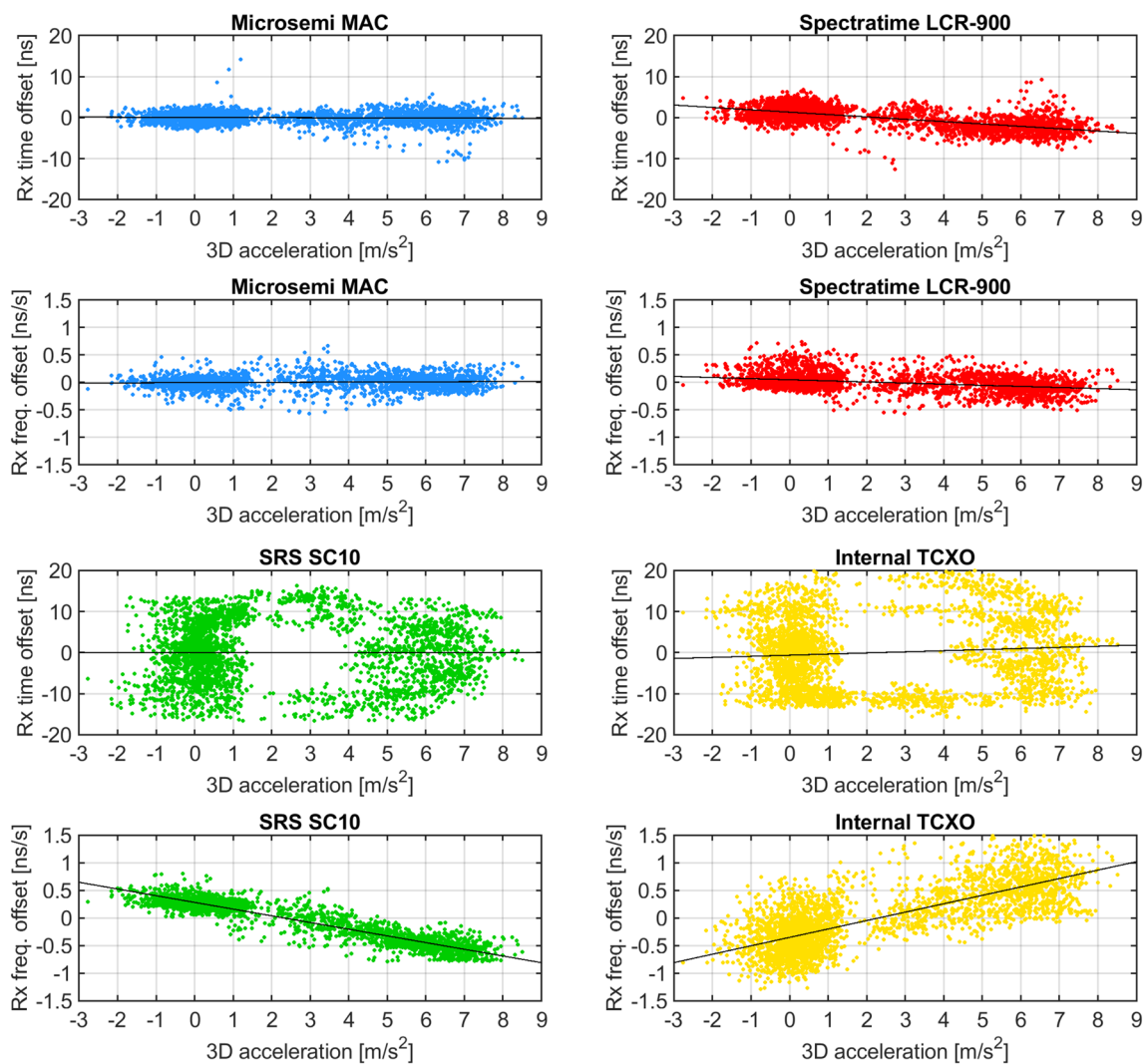


**Fig. 15** Receiver clock biases (time offset, frequency offset) of all receivers in flight segment F-G as a function of aircraft acceleration, where the black lines indicate characteristic curves between both axes

## Conclusions

We presented and discussed individual characterizations of the frequency stability of two miniaturized rubidium clocks (Microsemi MAC SA.35m and Spectratime LCR-900) and one high-precision quartz oscillator (SRS SC10). The underlying comparison measurements were carried out at Physikalisch-Technische Bundesanstalt, Germany's national metrology institute. Based on these investigations, it was found that the individual Allan deviations agree well with manufacturer's data or even exceed those specifications, like in case of the Microsemi MAC. In addition, spectral density coefficients for application in a Kalman filter process noise model were derived for each oscillator. The SRS SC10 quartz oscillator was also studied regarding its temperature sensitivity. Here, an increase in

temperature led to a decrease in the oscillator frequency. However, no characteristic curve was evident for this dependency.

Following these investigations in a static laboratory environment, the three oscillators were applied in a flight experiment. The impact of flight turbulence at different altitudes could be seen from the noise levels of the estimated clock frequency offsets of the GNSS receivers connected to the oscillators. The frequency stability of the Microsemi MAC and the Spectratime LCR-900 is degraded by about one order of magnitude, while the stability of the SRS SC10 is degraded by about two orders or magnitude compared to the static laboratory environment. In order to consider this degradation in a Kalman filter navigation solution, the spectral coefficients of the clock process noise can be adapted according to accelerations. Also, the impact of flight dynamics on the performance of the oscillators was investigated. It

was found that steep turn maneuvers with accelerations of up to  $9 \text{ m/s}^2$  cause significant frequency shifts in the SRS SC10 and a receiver driven by its internal quartz oscillator of ca.  $-1.2 \times 10^{-9}$  and  $+1.5 \times 10^{-9}$ , respectively. Contrary to this, the atomic clocks do not show such behavior, since they are less g-sensitive within the experienced range of accelerations. Thus, for these oscillators, receiver clock modeling is feasible to strengthen the navigation performance even in high dynamics. In the case of SRS SC10, however, clock modeling would only work in low-dynamic applications.

**Acknowledgements** This work has been funded by the German Federal Ministry for Economic Affairs and Energy following a resolution of the German Bundestag (Project Number: 50NA1705). The authors would like to thank Dr. Jens Kremer and Andreas Dach from IGI mbH for conducting the flight experiment with us and providing the reference trajectory solution. Furthermore, we thank our reviewers for their valuable and helpful suggestions and remarks, which helped to improve this article. Ankit Jain is an associated member of the DFG research training group i.c.sens to which he is really thankful.

**Funding** Open Access funding enabled and organized by Projekt DEAL.

**Data availability** All data included in this paper are available upon reasonable request by contact with the corresponding author.

**Open Access** This article is licensed under a Creative Commons Attribution 4.0 International License, which permits use, sharing, adaptation, distribution and reproduction in any medium or format, as long as you give appropriate credit to the original author(s) and the source, provide a link to the Creative Commons licence, and indicate if changes were made. The images or other third party material in this article are included in the article's Creative Commons licence, unless indicated otherwise in a credit line to the material. If material is not included in the article's Creative Commons licence and your intended use is not permitted by statutory regulation or exceeds the permitted use, you will need to obtain permission directly from the copyright holder. To view a copy of this licence, visit <http://creativecommons.org/licenses/by/4.0/>.

## References

- Allan D (1987) Time and frequency (time-domain) characterization, estimation, and prediction of precision clocks and oscillators. *IEEE Trans Ultrason Ferroelectr Freq Control* 34(6):647–654
- Barnes J, Chi A, Cutler L, Healey D, Leeson D, McGunigal T, Mullen J, Smith W, Sydnor R, Vessot R, Winkler G (1971) Characterization of frequency stability. *IEEE Trans Instrum Meas* 20(2):105–120
- Böhm J, Werl B, Schuh H (2006) Troposphere mapping functions for GPS and very long baseline interferometry from European Centre for Medium-Range Weather Forecasts operational analysis data. *J Geophys Res Solid Earth*. <https://doi.org/10.1029/2005JB003629>
- Filler R (1988) The acceleration sensitivity of quartz crystal oscillators: a review. *IEEE Trans Ultrason Ferroelectr Freq Control* 35(3):297–305. <https://doi.org/10.1109/58.20450>
- Hati A, Nelson C, Howe D (2009) Vibration-induced PM noise in oscillators and its suppression. In: Lam T (ed) *Aerial vehicles*. IntechOpen, Rijeka, pp 259–286. <https://doi.org/10.5772/6476>
- IGI (2020) AEROcontrol—GNSS/IMU Navigation System. Integrated Geospatial Innovations. <https://www.igi-systems.com/aerocontrol.html>.
- Irsigler M, Eissfeller B (2002) PLL tracking performance in the presence of oscillator phase noise. *GPS Solut* 5(4):45–57. <https://doi.org/10.1007/PL00012911>
- Jain A, Schön S (2019) Simulation studies to evaluate the impact of receiver clock modelling in flight navigation. *Frontiers of Geodetic Science*, Stuttgart. <https://doi.org/10.15488/5367>
- Johnston G, Riddell A, Hausler G (2017) The International GNSS Service. In: Teunissen P, Montenbruck O (eds) *Springer handbook of global navigation satellite system*. Springer, Cham, pp 967–982
- Kasdin N (1995) Discrete simulation of colored noise and stochastic processes and  $1/f^\alpha$  power law noise generation. *Proc IEEE* 83(5):802–827. <https://doi.org/10.1109/5.381848>
- Knable N, Kalafus R (1984) Clock coasting and altimeter error analysis for GPS. *Navigation* 31(4):289–302. <https://doi.org/10.1002/j.2161-4296.1984.tb00880.x>
- Krawinkel T, Schön S (2014) Application of miniaturized atomic clocks in kinematic GNSS single point positioning. In: *Proceedings of the 28th European Frequency and Time Forum*, pp 97–100
- Krawinkel T, Schön S (2016) Benefits of receiver clock modeling in code-based GNSS navigation. *GPS Solut* 20:687–701
- Krawinkel T (2018) *Improved GNSS Navigation with Chip-scale Atomic Clocks*. Dissertation, Leibniz University Hannover. <https://doi.org/10.15488/4684>
- Krawinkel T, Schön S (2018) On the potential of receiver clock modeling in kinematic precise point positioning. In: *Proceedings of the ION GNSS+ 2018*, Institute of Navigation, Miami, Florida, USA, September 24–28, 3897–3908.
- Microsemi (2018) *Chip-Scale Atomic Clock (CSAC) Performance during rapid temperature change*. White Paper. [https://www.microsemi.com/document-portal/doc\\_download/1243735-csac-performance-during-rapid-temp-change](https://www.microsemi.com/document-portal/doc_download/1243735-csac-performance-during-rapid-temp-change).
- Misra P, Pratt M, Burke B, Ferranti R (1995) Adaptive modeling of receiver clock for meter-level DGPS vertical positioning. In: *Proceedings of the ION GPS 1995*, Institute of Navigation, Palm Springs, CA, USA, September 12–15, 1127–1135
- Montenbruck O et al (2017) The multi-GNSS experiment (MGEX) of the International GNSS Service (IGS)—achievements, prospects and challenges. *Adv Space Res* 59(7):1671–1697
- Riley W (2008) *Handbook of frequency stability analysis*. NIST Special Publication 1065
- Spectratime (2014) *Ultra Low Cost Rubidium (LCR-900)*. Data sheet. [https://crystal.ru/pdf/SpectraTime/iSource\\_LCR-900\\_Spec.pdf](https://crystal.ru/pdf/SpectraTime/iSource_LCR-900_Spec.pdf).
- Sturza M (1983) GPS navigation using three satellites and a precise clock. *Navigation* 30(2):146–156. <https://doi.org/10.1002/j.2161-4296.1983.tb00831.x>
- Teunissen P (1997) Minimal detectable biases of GPS data. *J Geod* 72:236–244
- Van Graas F, Craig S, Pelgrum W, Ugazio S (2013) Laboratory and flight test analysis of rubidium frequency reference performance. *Navigation* 60(2):123–131. <https://doi.org/10.1002/navi.34>
- Vig J, et al. (1992) Acceleration, vibration and shock effects—IEEE standards project P1193. In: *Proceedings of the 1992 IEEE frequency control symposium*, Hershey, PA, May 27–29, 763–781
- Ward P, Betz J, Hegarty C (2006) Satellite signal acquisition, tracking, and data demodulation. In: Kaplan E, Hegarty C (eds) *Understanding GPS: principles and applications*, 2nd edn. Artech House, Norwood, pp 153–241
- Weinbach U, Schön S (2011) GNSS receiver clock modeling when using high-precision oscillators and its impact on PPP. *Adv Space Res* 47:229–238

**Publisher's Note** Springer Nature remains neutral with regard to jurisdictional claims in published maps and institutional affiliations.



**Ankit Jain** obtained his doctorate degree in Telecommunications from IMT Atlantique (formerly known as Telecom Bretagne) in January 2019. Since May 2019, he is working as a research assistant in the positioning and navigation group of the Institut für Erdmessung (IfE) at Leibniz University Hannover (LUH). He is involved in GNSS software development, data analysis and experimentation. His current work is mainly related to GNSS receiver clock technologies.



**Thomas Krawinkel** has a background in Geodesy and Geoinformatics and is a postdoc in the positioning and navigation department of IfE at LUH. He is involved in software development and GNSS data analysis, particularly focusing on kinematic applications. His current research interests include Kalman filtering as well as receiver and clock technology.



**Steffen Schön** is a professor for positioning and navigation at IfE since 2006. His research interests are the correction and assessment of systematic errors in GNSS, absolute antenna calibration, receiver clock modeling and improved stochastic models for GNSS observations based on turbulence theory. He is also currently the spokesman of the DFG research training group integrity and collaboration in dynamic sensor networks (i.c.sens) working on interval mathematics for integrity and collaborative

navigation.



**Andreas Bauch** received a PhD in Physics and joined Physikalisches Technische Bundesanstalt (PTB), Braunschweig, Germany, in 1983. He is involved in time and frequency metrology, focusing at first on the development and operation of atomic clocks and later on time comparison techniques (GNSS, TWSTFT). Today, he is Head of PTB's Time Dissemination Working Group and, as such, has management responsibility for the operation of PTB's time dissemination services.